American Journal of Astronomy and Astrophysics
2021; 9(3): 32-41
http://www.sciencepublishinggroup.com/j/ajaa
doi: 10.11648/j.ajaa.20210903.12
ISSN: 2376-4678 (Print); ISSN: 2376-4686 (Online)

Jupiter and Saturn Multi-layer Models Rotating Differentially

Joel Uriel Cisneros-Parra[1, 2, *], Francisco Javier Martinez-Herrera[2], Daniel Montalvo-Castro[2]

[1]Sciences Faculty, Autonomous University of San Luis Potosí, San Luis Potosí, Mexico

[2]Physics Institute, Autonomous University of San Luis Potosí, San Luis Potosí, Mexico

Email address:

cisneros@galia.fc.uaslp.mx (J. U. Cisneros-Parra), marherrera@fciencias.uaslp.mx (F. J. Martinez-Herrera), montalvo@ifisica.uaslp.mx (D. Montalvo-Castro)

[*]Corresponding author

To cite this article:

Joel Uriel Cisneros-Parra, Francisco Javier Martinez-Herrera, Daniel Montalvo-Castro. Jupiter and Saturn Multi-layer Models Rotating Differentially. *American Journal of Astronomy and Astrophysics*. Vol. 9, No. 3, 2021, pp. 32-41. doi: 10.11648/j.ajaa.20210903.12

Received: July 2, 2021; **Accepted**: July 19, 2021; **Published**: July 27, 2021

Abstract: In a past work, models for Jupiter were constructed in base to a set of concentric distorted spheroids ("spheroidals") rotating differentially—whose semi-axes are independent of one another—a task that was achieved with a law of rotation deduced from a generalization of Bernoulli's theorem, and which holds exclusively for axial-symmetric masses. The shape of the mass is that of a spheroid whose surface equation contains an extra term, d/z^4, where d is a parameter which measures the degree of distortion. Each layer rotates with its own profile of angular velocity. The rotation law has a simple dependence on the derivative of the gravitational potential. No magnetic fields or equations of state were involved. The multi-structures were demanded, firstly, to reproduce the gravitational moments of the planets, as surveyed by space missions; and, secondly, to be equilibrium figures. For the calculation of the gravitational moments, a minimization procedure was employed. Paying attention on the outermost laye—the relevant one in the present context—of the formerly reported models for Jupiter, we became aware that they all share an angular velocity profile that decreases from the pole towards the equator, an event that, so far, has not been verified observationally**.** Since figures with profiles of the opposite tendency turned out to be also possible, they should be included as candidates for our purpose, as effectively they are herein as a complement of that work. The same procedure is here entailed to Saturn, for which figures to show one or the other tendencies are as well obtained. The dual behavior of the rotation profiles may be explained by arguments involving the centripetal force. According to this standpoint, the double behavior is a consequence of the algebraic sign assigned to d: if positive, so that the surface is more bloated than that of a spheroid, the decreasing tendency results; whereas if negative, so that the surface is more depressed, the increasing tendency shows up. This, in turn, is because for d negative the radial force increases more rapidly from pole to the equator than for d positive. We point out that the rotation profiles of the current figures are determined from their equilibrium, rather than being imposed *ad initio*.

Keywords: Gravitation, Hydrodynamics, Planets and Satellites: General, Stars: Rotation

1. Introduction

In papers [1, 2], models for Jupiter were constructed consisting of a set of concentric distorted spheroids ("spheroidals"), each of constant density and rotating with its own distribution of differential angular velocity. The demands were, firstly, that the gravity moments J_{2n}, as calculated theoretically, agree with those surveyed by the Juno mission; and, secondly, that they be equilibrium figures.

The equilibrium is sustained by gravitation, pressure, and rotation. The study here concerns exclusively to axial-symmetric masses; ellipsoids with three unequal axes are not allowed, either distorted or not. In particular, the outermost shell of the models (on which the attention is focused) rotates, generally, differentially, with the pole running faster than the equator.

On the other hand, it is well-known that in the Sun the opposite tendency occurs [3]. This type of models are presented here for Jupiter, thus complementing the work on that planet.

For Saturn, both types of models are also possible. The kind of models that better describes the two planets must be decided by observational means. Direct observations of Saturn's local motions are the zonal winds [4, 5]. Measurements of the velocity field v (taken between *2004* and *2009*) from the Cassini-Saturn images at the northern hemisphere are plotted in Figure 1.

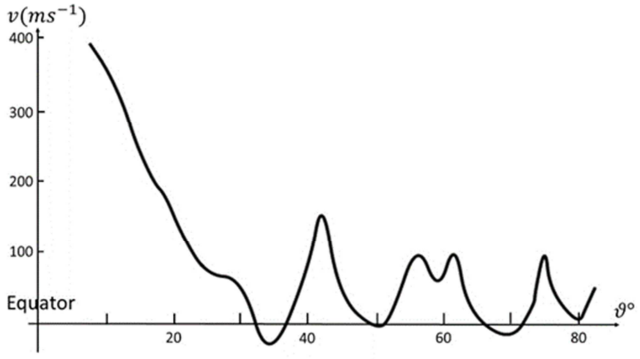

Figure 1. *Zonal wind profile for Saturn measured by the Cassini mission between 2004 and 2009, according to [5].* $\boldsymbol{v}$ *is the velocity in* ms^{-1}*, and* ϑ *is the latitude in degrees.*

Supposing this motion comes from rotation, the angular velocity $\omega(R) = v/R$ can be deduced, where R is the distance from the rotation axis ($\vartheta = 90°$). To establish R at each latitude ϑ, take as surface the equation z (R) of the models (see section 4.2), so that $R = z(R/\tan\vartheta)$. The last relation allows getting R for each latitude. The rotational profile can consequently, be constructed, as shown in Figure 2.

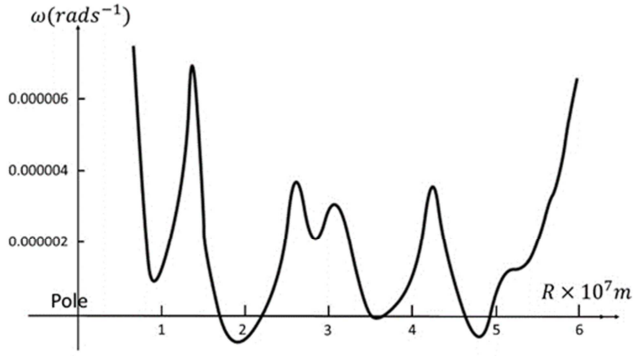

Figure 2. *Saturn's angular velocity profile* $\omega(R)$ *deduced from the velocity field of Figure 1. R is the distance from the rotation axis (R=0).*

In Figure 2, it is seen that the angular velocity does not follow a definite tendency, either increasing or decreasing. Since in former models, as well as in those presented here, ω can increase or decrease from pole to the equator, the observed motions (below about *1 bar*), although persistent, cannot be explained by our equilibrium figures. Moreover, the angular velocities depicted in Figure 2 are about one order of magnitude lower than the commonly values taken for Saturn [6], which are in accordance with our models. Information regarding deeper layers, rather than just at the atmospheric level, is required. In fact, the models predict rotation profiles that decrease in magnitude from the core outwards.

In building the models, we suppose a core with a size of one-tenth of the planet radius, as in Gudkova's study [7]. Certainly, this is not a necessary constraint for the procedure, and can be omitted, or replaced by any other. Of course, the external pressure is zero on the outermost shell (not named atmosphere here), but it may be substituted by any other constant value without essential changes.

The planet model is constructed now by assuming that it comprises l layers of constant density each, approaching a continuous density distribution. The outermost layer must have the known polar and equatorial radii of the planet. Density and shape of the layers are established by demanding that the mass distribution reproduces the observed gravitational field of the planet. By requiring equilibrium of the model, a rotation state is found that allows it. Each shell has its own rotation profile, it being a result from the equilibrium, rather than being constrained from the beginning. In this procedure, we are not proposing or testing any particular chemical composition of the shells, nor seeking for a correct equation of state that could eventually lead to a temperature dependence. Hence our model may be applied to the Sun and stars. The purpose is to find the mass distribution that generates the known gravitation, which is independent of a special matter type or state equations. Knowledge of the density distribution might be a hint for structure researching for planets and stars, which usually assumes spherical symmetry. We do not claim that our models are unique, but imposing to them additional constraints taken perhaps from structure studies or other sources, they can correspond better to reality. For instance, Gudkova worked out a structure model for a planet supposing an ice-rock core of a certain size and mass, restriction that we imposed to our models. This is an example of how constraints taken from structure models can be implanted into the models.

2. Theoretical Background

In a previous work [8], the basis for studying equilibrium of a stratified mass in the state of rotation has been exposed at length; we summarize it here for the sake of a quick reference. The term equilibrium is used in this paper (and in the cited reference) as a synonymous with steady-state: the mass retains its shape despite the motion of each of its points. The shape (of the total mass and individual shells) is assumed to be of a known type, namely, a distorted spheroid with surface equation:

$$\frac{x^2+y^2}{e_e^2} + \frac{z^2}{e_n^2} + d\frac{z^4}{e_n^4} = 1 \qquad (1)$$

where e_e is the equatorial radius, d the measure of the surface's distortion (not restricted to be low), and e_n is a quantity related to the polar radius z_p through:

$$z_p = e_n \sqrt{\frac{\sqrt{4d+1}-1}{2d}} \quad (2)$$

Although d is not limited to small values, it has a mathematical constraint: $d > -1/4$. The figure's volume τ can be established analytically:

$$\tau = \frac{2\pi(12d-\sqrt{4d+1}+1)e_e^2 z_p}{15d} \quad (3)$$

Moreover, taking as reference a spheroid (d=0), its volume $4\pi\, e_e^2\, z_p/3$ lies between the volumes of those two cases. In other words, for positive d the spheroidal is more bloated than the spheroid, whereas for negative d it is more depressed, as depicted in Figure 3.

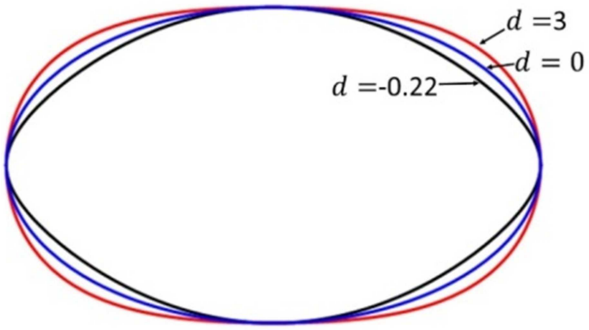

Figure 3. *Three graphs from equation (1), using the same polar and equatorial radii. Since the figures are axial-symmetric, only the x-z sections are depicted. The d > 0 spheroidal (red line) is more bloated than the spheroid (blue line). Conversely, the d < 0 spheroidal (black line) is more depressed than the spheroid.*

The equilibrium of the masses is based on a generalization of Bernoulli's theorem [1, 2, 9], which establishes that, for a stream-line, the following relation holds

$$\frac{1}{2}\, v^2 - V + \frac{1}{\rho}\, p = \text{k} \quad (4)$$

where $\boldsymbol{v}$ is the velocity field, V the gravitational potential, p the pressure, ρ the (constant) density, and k a constant. Assume that $\boldsymbol{v}$ is due to a rotation with angular velocity ω about the z-axis Hence, the velocity is expressed as

$$v = (-y, x, 0)\omega \quad (5)$$

where the parenthesis represents a vector with Cartesian components –y, x, 0. The continuity equation, $\nabla \cdot \boldsymbol{v}$=0, puts a restriction on the dependence of ω on x, y, z [10]:

$$\omega = \omega(x^2 + y^2, z) \quad (6)$$

Essentially, k is constant for a particular streamline, but not for everyone. It is the same constant only if the motion is irrotational. In general, k must change [1, 6, 10] according to the relation

$$\nabla\, k = \boldsymbol{v} \times (\nabla \times\, \boldsymbol{v}) \quad (7)$$

Since the problem has cylindrical symmetry, it is more convenient to use cylindrical coordinates (R, φ, z). In this system, the velocity has only a φ component (tangent to circles centered on the z-axis):

$$\boldsymbol{v} = (0, R, 0)\omega \quad (8)$$

Therefore, the components of equation (7) are

$$\frac{\partial k}{\partial R^2} = (R^2\, \frac{\partial \omega}{\partial R^2} +\, \omega)\omega$$

$$\frac{\partial k}{\partial z^2} = R^2 \omega \frac{\partial \omega}{\partial z^2} \quad (9)$$

Equations (9) can be solved generally, with the result [1, 2, 9]

$$k = \frac{1}{2}\, R^2\, \omega^2 + f(R^2), \quad \omega^2 = 2f'(R^2) \quad (10)$$

where f is an arbitrary function of R^2. Hence, ω depends, at most, on R^2, and must be constant on cylinders of radius R, whose axis is the rotation axis. Substituting the expression for k into Bernoulli's equation (4), one may determine the unknown function f:

$$-f\,(R^2) - V(R^2, z^2) + \frac{1}{\rho} p = 0 \quad (11)$$

As f depends on R but not on z, its evaluation requires only of the figure surface, on which it is assumed p=*0*:

$$f\,(R^2) = -V(R^2, z^2) \quad (12)$$

where in the gravitational potential V, z must be substituted by the surface equation, so that V becomes a function of R only. Knowing f, the angular velocity is established (see equation (10)):

$$\omega^2 = -2\frac{dV}{dR^2} \quad (13)$$

Whenever the body's shape is known, as it is the case here (equation (1)), the potential V can be calculated at any point, in particular, in the surface. By equation (12), ω is obtained, i.e., given a figure, there is only one angular velocity profile with which it can rotate; conversely, given a certain angular velocity profile, an arbitrary figure cannot be put in rotation (in equilibrium).

2.1. Multi-layer Structures

Consider now an axial symmetric mass distribution consisting of l shells with surfaces of the kind (1) and constant density ρ_i ($i = 1, \ldots, l$) each, ρ_1 being the density of the outermost layer. For any layer, the equilibrium equation (11) holds:

$$\frac{1}{\rho_i} p_i = f_i(R^2) + V_i(R^2, z^2) \quad (14)$$

where the last term is the total potential at the point (R, z) of the body; p_i the pressure at that point, and f_i is an unknown function. The f_i functions, l in total, are established by the boundary conditions at the several interfaces. At every point of surface: S_1: p_1=0; S_2: $p_1 = p_2, \ldots$; S_i: $p_l = p_{l-1}$, where it is assumed that no transfer of mass occurs between shells. The S_i surfaces are concentric, but otherwise independent of one another. Every surface equation is of the type $g(R, z^2) =$

0, so that solving for z, one gets $z=h(R)$, and all quantities in equation (14) depend on R only. Therefore, according to equation (14), and knowing that the potential is continuous, from the boundary conditions one has:

$$\frac{1}{\rho_1}\, p_1 \,= 0 = f_1\,(R^2)\, + V_1(R^2\,, z^2) \tag{15}$$

$$p_i = p_{i-1}\colon (\rho_i - \rho_{i-1})V_i + \rho_i f_i - \rho_{i-1} f_{i-1} = 0 \tag{16}$$

or

$$f_i = -\frac{\delta\rho_i}{\rho_i} V_i + \frac{\rho_{i-1}}{\rho_i} f_{i-1}, \quad f_1 = -V_1 \tag{17}$$

where $\delta\rho_i = \rho_i - \rho_{i-1}$ and $\delta\rho_1 = \rho_1$

Knowing the relation between ω_i and f_i (see second of equations (10)), equation (17) allows one to determine the angular velocity of each shell:

$$\omega_i^2 = -\frac{2\delta\rho_i}{\rho_i}\frac{dV_i}{dR^2} + \frac{\rho_{i-1}}{\rho_i}\omega_{i-1}^2,\ \omega_1^2 = -2\frac{dV_1}{dR^2} \tag{18}$$

Hence, for calculating the angular velocity of the i-th shell, the total potential at the interface S_i and ω of the layer immediately above are required. We can expect generally that the potential derivative is not constant on an interface, so that the angular velocity is necessarily of differential nature. Certainly, the potential is related to the geometry and the density distribution of the body in an involved fashion.

2.2. The Gravitational Moments

The gravitational field at external points of a mass distribution with density $\rho(r)$ is established if the gravitational moments are known. For an axis-symmetric configuration, they are even, and can be calculated by the following expression

$$J_{2n} = -(Ma^{2n})^{-1}\int_\tau \rho(r) r^{2n} P_{2n}\,(cos\vartheta) d\tau) \tag{19}$$

where M, a and τ are the mass, the equatorial radius, and the volume, respectively, of the body, P_{2n} the Legendre polynomials of order $2n$, and ϑ the colatitude measured from the pole to the equator. The integral (19) can be evaluated more easily using cylindrical coordinates, and noticing that $\rho(r) = \rho_i$ for all points of the ith shell. Therefore, (19) breaks into a sum of integrals over layers of constant density:

$$J_{2n} = -\rho_1(Ma^{2n})^{-1}\sum_{i=1}^{l} \varepsilon_i \times\int_{\tau_i}(R^2 + z^2)^n P_{2n}\left(\frac{z}{\sqrt{R^2+z^2}}\right) \times RdRd\varphi dz, (n = 1,2, \dots) \tag{20}$$

where ρ_1 is the density of the outermost shell, τ_i the volume limited by S_i, and ε_i the fractional relative density of the i-shell:

$$\varepsilon_i = \frac{\rho_i - \rho_{i-1}}{\rho_i} \tag{21}$$

with $\varepsilon_1 = 1$. Because the particular shape (1) of the shell surfaces, the integrals in (20) can be calculated exactly; they are given by

$$-\frac{\rho_i}{Ma^{2n}}\int_{\tau_i}(R^2 + z^2)^n P_{2n}\left(\frac{z}{\sqrt{R^2+z^2}}\right)\mathrm{RdRd}\varphi dz = f_{2n}\left(e_{1i,}\, z_{Mi,} d_i\right) \tag{22}$$

where the parameters of the i-th shell, e_{1i} and z_{Mi} are normalized to the equator radius a of the body:

$$e_{1i} = \frac{e_{ei}}{a},\ z_{Mi} = \frac{z_{pi}}{a} \tag{23}$$

The functions f_{2n} are given in Appendix A, they being reproduced from [1]. As a consequence of relations (20) and (22), the gravitational moments depend on $4l-2$ parameters: $e_{1i}, z_{Mi,} d_i, \varepsilon_i$ (i=1,..., l), and ε_1 =1, $z_{M1} = b/a$, where b is the known planet's polar radius. A figure of, say, ten layers needs 38 parameters to be specified in order to determine the J_{2n} all.

3. Numerical Procedure

The observational basis for constructing a model is the gravitational field measured near the surfaces of fluid planets (Jupiter, Saturn) by some space missions. From these measurements, the gravitational moments are deduced; the models intend to reproduce them. The relation between the J_{2n} and the $4l-2$ parameters of a model is certainly a complicated one, and numerical strategies are required to find them in order that the theoretical moments (20) replicate the observed ones. This approach was discussed at length in [2], and here is summarized for an easy reference. Let J_{2n}^o be the observed moments and J_{2n} the theoretical ones given by equation (20). We look then for a model which satisfies $J_{2n} = J_{2n}^o$, n=1,2,…, i.e., the necessary set of $4l-2$ parameters to be found; alternatively,

$$\sum_n (J_{2n} - J_{2n}^o)^2 = 0 \tag{24}$$

The gravitational moments, like any other observed quantity, have uncertainties, that we call δJ_{2n}^o, so that the variables fall within the interval

$$J_{2n}^o \pm \delta J_{2n}^o \tag{25}$$

within a given confidence range. Rather than using in (24) the central values J_{2n}^o, one generates a set of moments at random from the intervals (25) and the group of parameters $e_{1i}, z_{Mi}, d_i, \varepsilon_i$ for a model is found by a minimization procedure:

$$\min \sum_n (J_{2n} - J_{2n}^o)^2 \tag{26}$$

The models obtained this way are then tested for equilibrium, that is, one asks if angular velocities (18) are possible for the geometry and mass distributions achieved, finding that only a few models satisfy this demand.

4. Numerical Results

4.1. A Complement to Our Jupiter Multi-layer Model

We recall that our Jupiter study was begun with a two-

layer model [1], whose accuracy was not altogether satisfactory: the resulting J_6 was outside the confidence interval, and J_4 was near the limit. Otherwise, the model satisfied the equilibrium conditions and, further, was stable to second harmonics. Next the model was generalized to $l > 2$ concentric layers, onion-like assembled, and the technique described in section 3 was applied [2]. The procedure was supported by the known facts:

Equatorial radius: a=7.1492 × 10^7 m

Polar radius: b=6.6854 × 10^7 m

Period: T=9.92597 hrs.

Mass: M=1.89861 × 10^{27} Kg

and the observed gravitational moments taken from the Juno mission [11-13] (in units of 10^{-6}):

$$J_2=14697.3\pm0.0017,\ J_4=-\ 586.623\pm0.0024$$

$$J_6=34.244\pm0.0067,\ J_8=-\ 2.502\pm0.021 \quad (27)$$

In all these models, namely for l=2, and $l > 2$, the outermost layer had in common an angular velocity profile decreasing from the pole towards the equator, and the corresponding mean period was reasonably near the known value for Jupiter.

Now, it is well-known that the Sun rotates differentially with an angular velocity that increases from the pole towards the equator [3]. This fact, along with a lack of precise knowledge on Jupiter rotation state, motivated us to search for more models, this time with an increasing tendency. The restrictions were again to reproduce the gravitational moments (27), and to be equilibrium figures. The mean rotation period was an additional restriction. The task was successful. For l=2, two new models were constructed: one with ω increasing from pole to the equator (Model 1, Table 1), and the other with opposite tendency. (Model 2, Table 1). In both models, the cores are large (70% of Jupiter equator), and have wide envelopes; the density increase inwards about ten times. In these figures, the densities are seen as mean values of more elaborated models A characteristic distinction of these models is the shape. Both have the same polar and equatorial radii, but the distortion parameter is negative in one, and positive in the other (Table 1). Hence, the second is more bloated than the first (Figure 3). In the depressed figure, the radial gravitational force increases faster from pole to the equator than in the bloated one, which help to explain the increasing tendency; and conversely. This point of view is discussed in more detail in section 4.2. For Model 1, the calculated moments are (in units of 10^{-6}):

$$J_2=14696.4,\ J_4=-\ 586.703$$

$$J_6=34.236,\ J_8=-\ 2.454 \quad (28)$$

These values are within the error bars. For Model 2, we have

$$J_2=14696.5,\ J_4=-\ 5\ 86.674$$

$$J_6=34.525,\ J_8=-\ 2.591 \quad (29)$$

Table 1. *Normalized equatorial radius R_e; shell density ρ; equatorial pressure p_e; equatorial and polar angular velocity ω_p and ω_e; and mean period T_m of the surface, for two-layer models 1 (increasing ω in first shell) and 2 (decreasing ω in $first\ shell$) for Jupiter. Surface distortion parameter d is also indicated.*

R_e	ρ	p_e	ω_p	ω_e	T_m
norm	**Kgm $^{-3}$**	**Mbar**	**10^{-4}rad/s**	**10^{-4}rad/s**	**hr**
	Model 1		$d = -0.00695$		
.000		*0.0*	*1.728*	*1.785*	*9.93*
	358.1				
.700		22.0	1.914	1.956	
	3160.4				
	Model 2		$d = 0.00011$		
.000		*0.0*	*1.796*	*1.722*	*9.93*
	428.8				
.699		35.2	2.244	2.487	
	3021.4				

A multi-layer model with increasing ω is given in Table 2. The mean period is alike as in the two-layer case, yet figures with shorter ones were also found, but discarded for the current study. There are jumps in the density of the second shell, and thereafter it increases approximately linearly towards the center [1, 7]. The shells rotate differentially, but ω deviates little from solid-body rotation; from the second layer inwards, it increases regularly.

Another model with decreasing ω is given in Table 3. The first shell is relatively narrower than the second one, and its density is about 25 times smaller than the central one; here, ρ has also a linear behavior. The angular velocity at the outermost surface decreases from pole to the equator, and the mean period is similar to that of previous cases. In the deeper layers, ω is nearly constant, and increases towards the center.

The basic difference between the models of Table 2 and Table 3 is, once more, the shape: Model 3 (d negative) is depressed, while Model 4 (d positive) is bloated. Hence, ω increases from pole to the equator at the outermost surface of the first, and conversely for the second. Therefore, one can decide, at least qualitatively, if Jupiter rotates with one or the other profile, that is, if the planet is bloated or depressed with respect to a spheroid.

Table 2. *Normalized equator radius R_e; shell density ρ; equatorial pressure p_e; polar and equatorial angular velocity ω_p and ω_e; and mean period T_m of the surface, for multi-layer model 3 (increasing ω in first shell) of Jupiter. Surface distortion parameter d is also indicated.*

R_e	ρ	p_e	ω_p	ω_e	T_m
norm	**Kgm $^{-3}$**	**Mbar**	**10^{-4} rad/s**	**10^{-4}rd/s**	**hr**
	Model 3		$d = -0.0054$		
.000		*0.0*	*1.740*	*1.773*	*9.94*
	32.6				
.905		2.42	1.198	1.261	
	1707.9				
.815		8.02	1.314	1.282	
	1728.0				
.768		8.52	1.367	1.303	
	1739.8				
.666		16.35	1.572	1.522	
	1763.6				
.588		17.10	1.931	1.875	
	1813.8				
.495		17.22	2.176	2.134	
	1856.0				
.426		17.06	2.270	2.232	
	1874.0				
.362		17.12	2.347	2.316	
	1889.5				
.304		17.36	2.518	2.490	
	1927.9				
.250		17.52	2.707	2.676	
	1974.6				
.203		17.47	2.831	2.810	
	2007.2				
.162		17.54	2.968	2.950	
	2046.3				
.127		17.43	3.052	3.041	
	2071.8				
.100		17.43	3.128	3.118	
	2096.3				
.000					

Table 3. *Normalized equator radius R_e, shell density ρ, pressure p_e at equator, angular velocity ω_p and ω_e in pole and equator and mean period T_m of the surface, for multi-layer model 4 (decreasing ω first shell) of Jupiter. Surface distortion parameter d is also indicated.*

R_e	ρ	p_e	ω_p	ω_e	T_m
norm	**Kgm $^{-3}$**	**Mbar**	**10^{-4} rad/s**	**10^{-4}rd/s**	**hr**
	Model 4		$\boldsymbol{d = 0.0048}$		
.000		*0.0*	*1.840*	*1.677*	*9.93*
	101.5				
.921		2.42	1.073	1.107	
	1566.8				
.788		4.42	1.343	1.111	
	1613.0				
.689		7.21	1.620	1.579	
	1646.4				
.597		10.3	2.485	2.411	
	1786.5				
.510		12.4	2.939	2.823	
	1901.7				
.430		14.4	3.294	3.152	
	2026.1				
.356		15.5	3.463	3.366	
	2088.3				
.288		17.4	3.790	3.727	
	2229.1				
.228		18.2	4.049	4.011	
	2353.7				
.176		18.1	4.103	4.080	
	2381.6				
.133		18.8	4.207	4.191	
	2438.2				
.100		19.2	4.330	4.320	
	2510.3				

4.2. Saturn Models

Attempts for building giant planet models can be found elsewhere. Recent observed facts are used in the structure equations that, commonly, are solved supposing spherical symmetry, from which there result a set of physical variables depending on the radius *r*; in particular, the density at each point is established: $\rho = \rho(r)$. However, there are cases in which the results are expressed in terms of the pressure p: $\rho = \rho(p)$. Although any of the two representations can be used [5], it is more direct to take the density's *r*-dependence. There are Saturn (and also Jupiter) models [7, 13] in which the density is (graphically) given, in terms of the distance from the center. In them, the density increases almost linearly from the outermost surface to the core (normalized r ≈ 0.1), where it makes a jump to remaining constant thereafter. Here, the constructed models differ from the two cited ones in some aspects: they rotate, do not possess spherical symmetry, and do not assume any chemical composition or a particular equation of state. The aim is mainly to establish a mass distribution and a rotation profile that may explain the observed gravitational field. Yet, it is intended that they be related to structure (spherical) models by constraining our figures to have an approximately linear density distribution in a wide part of them. As always, we demand that the models, besides of duplicating the observed gravitational moments, be equilibrium figures, and that the mean rotation period be close enough to the accepted one. Moreover, the Saturn models are sustained by the known relevant facts:

Mass: $M_S = 5568319 \times 10^{21}$Kg

Polar radius: b=60268000 m

Equatorial radius: a=54364000 m

And the gravitational moments surveyed by the Cassini mission (in units of 10^{-6}) [14]:

$$J_2=16.290.573\pm0.028,\ J_4=-\ 935.314\pm0.037$$

$$J_6=86.340\pm0.087,\ J_8=-\ 14.624\pm0.205 \quad (30)$$

As in the case of Jupiter, we constructed Saturn models by, in a first step, randomly generating sets of J_{2n} (within the error bars), and then determining the geometrical shape of the shells and their respective densities. Next, the obtained figures were tested for equilibrium, only a few of them meting this requirement. That is, an angular velocity distribution sustaining the equilibrium could be found for a few models. Furthermore, the mean value of the outermost surface of these figures seldom agrees with the observed one. Two models satisfying the whole restrictions were found: the first (Model 5, Table 4) with negative *d*; and the other (Model 6, Table 5) with *d* positive. In both cases, the mean period T_m is, approximately, the observed one. T_m was calculated from the mean angular velocity at the outermost surface, given by

$$\omega_m = \int_0^1 \omega(R)dR \quad (31)$$

In Tables 4 and 5, one sees that ω increases from pole to the equator for $d < 0$ (> -1/4); but it gets backwards for $d > 0$. Once more, we have that, if the figure is more depressed than the spheroid, ω increases from the pole to the equator. On the contrary, if the figure is more bloated than the spheroid, the tendency is reversed. To get an idea about how this process can happen, we constructed from each of the two heterogeneous models a mean homogeneous figure having as equatorial and polar radii the mean value of the corresponding radii of the shells, and as distortion parameter the mean value of that of the shells. That is

$$e_m = \frac{\int_\tau R_e \rho d\tau}{\int_\tau \rho d\tau} = \frac{R_{e1}\sum_{i=1}^{l} R_{ei}\varepsilon_{ei}\int_{\tau_i} d\tau}{\sum_{i=1}^{l} \varepsilon_i \int_{\tau_i} d\tau}$$

$$z_m = \frac{z_{p1}\sum_{i=1}^{l} z_{pi}\varepsilon_{zi}\int_{\tau_i} d\tau}{\sum_{i=1}^{l} \varepsilon_i \int_{\tau_i} d\tau} \quad (32)$$

$$d_m = \frac{d_1\sum_{i=1}^{l} d_i\varepsilon_{di}\int_{\tau_i} d\tau}{\sum_{i=1}^{l} \varepsilon_i \int_{\tau_i} d\tau}$$

where

$$\varepsilon_{ei} = \frac{\rho_i R_{ei} - \rho_{i-1}R_{ei-1}}{\rho_1 R_{e1}}, \varepsilon_{zi} = \frac{\rho_i z_{pi} - \rho_{i-1}z_{pi-1}}{\rho_1 R_{e1}}$$

$$\varepsilon_{di} = \frac{\rho_i d_i - \rho_{i-1}d_{i-1}}{\rho_1 R_{e1}}, \varepsilon_i = \frac{\rho_i - \rho_{i-1}}{\rho_1} \quad (33)$$

From relations (32) and (33), for d=– 0.030, we find

$$e_m = 0.5413, z_m = 0.3256,\ d_m = 0.0549 \quad (34)$$

And, for d=0.020:

$$e_m = 0.5357, z_m = 0.3223, d_m = 0.0478 \quad (35)$$

Models (34) and (35) are oblate ($e_m > z_m$) and they are quite similar (since they are related to the same planet). Let these figures be surrounded by surfaces identical to those of the corresponding heterogeneous models. Because the models are oblate, the radial force exerted at each point of the surfaces must increase from the pole to the equator, the force increasing more rapidly on the depressed (nearer to the mean model) surface than at the bloated one (farther than the mean model).

Next, the radial force dV/dR implied in equation (13) is calculated at each point of the surface of the planet's model (first row of Tables 4 and 5). The numerical method supplies the force (calculated from a potential V normalized to $G\rho_1 a^2$) at discrete points and, for easy handling, we approximate it by a quadratic function. We find

$$f_{-.03}=14.405R + 2.521\ R^2$$

$$f_{.02}=18.940R - 6.212\ R^2 \quad (36)$$

All shells were constrained to be oblate, hence the resulting mean figure is oblate. Therefore, the radial force increases from pole (R=0) to the equator (R=1), the rate of increasing being higher for d=– 0.0030 (depressed surface) than for d=0.020 (bloated surface). However, prolate layers are also possible (rotation axis being larger than the equatorial one), so that if the model is worked out with such

shapes, the external force will be decreasing from pole to the equator.

From equation (13), we can deduce the angular velocity (we call $\Omega=\omega^2(G\rho_1)^{-1}$ the normalized angular velocity) at the surface:

$$\Omega_{-30}=14.405+2.521\ R$$

$$\Omega_{20}=18.940-6.212\ R \qquad (37)$$

It is easily seen that the angular velocity increases from the pole to the equator for $d=-0.0.030$, whereas it decreases for $d=0.020$. The distortion parameter d plays an important role in the resulting angular velocity profile at the outermost surface of the planet. In order to see this more clearly, let us interchange the surfaces of the two models, so that the first becomes an envelope with $d=0.020$, and the second an envelope with $d=-0.030$, but otherwise letting the shells and densities untouched. Calculating the forces at points of the new envelopes, one has

$$f^*_{-.03}=18.4489R-5.959R^2$$

$$f^*_{.02}=14.793R+2.473R^2 \qquad (38)$$

and from here it can be deduced that the angular velocity profiles are also interchanged (although not numerically). That is, the same mass distribution gives rise to a greater radial force at a depressed (nearer to the rotation axis) surface than at a bloated one.

Table 4. *Normalized equator radius R_e and polar radius z_p, shell density ρ, angular velocity ω_p and ω_e in pole and equator and mean period T_m of the surface, for multi-layer Saturn Model 5 (increasing ω in first shell). Surface distortion parameter d is also indicated.*

R_e	z_p	ρ	ω_p	ω_e	T_m
norm	**norm**	**Kgm $^{-3}$**	**10^{-4} rad/s**	**10^{-4}rad/s**	**hr**
	Model 5		**$d=-0.030$**		
.000	*0.902*	*26.50*	*1.555*	*1.725*	*10.533*
.931	0.901	723.03	0.581	0.476	
.907	0.751	747.06	0.808	0.356	
.864	0.515	760.96	0.960	0.690	
.818	0.416	776.83	1.149	0.900	
.732	0.416	814.35	1.426	1.233	
.651	0.415	832.79	1.527	1.345	
.617	0.376	861.06	1.682	1.450	
.573	0.351	899.84	1.835	1.647	
.500	0.324	914.71	1.889	1.719	
.432	0.289	937.17	1.972	1.785	
.407	0.262	960.94	2.045	1.859	
.368	0.228	975.71	2.090	1.942	
.308	0.180	996.79	2.159	2.054	
.255	0.119	1015.5	2.229	2.151	
.239	0.100	1038.0	2.312	2.242	
.206	0.089	1091.5	2.494	2.406	
.164	0.067	1115.7	2.566	2.515	
.128	0.045	1141.5	2.646	2.607	
.100	0.012	1165.5	2.728	2.710	

Table 5. *Normalized equator radius R_e and polar radius z_p, shell density ρ, angular velocity ω_p and ω_e in pole and equator and mean period T_m of the surface, for multi-layer Saturn Model 6 (decreasing ω first shell). Surface distortion parameter d is also indicated.*

R_e	z_p	ρ	ω_p	ω_e	T_m
norm	**norm**	**Kgm $^{-3}$**	**10^{-4}rad/s**	**10^{-4}rad/s**	**hr**
	Model 6		**$d=0.020$**		
.000	*0.901*	*25.87*	*1.834*	*1.486*	*10.543*
.921	0.885	740.3	0.540	0.894	
.877	0.872	775.6	0.673	0.514	
.864	0.639	798.6	0.887	0.672	
.818	0.513	810.4	1.004	0.850	
.732	0.426	828.6	1.168	1.034	
.651	0.333	858.9	1.426	1.264	
.617	0.327	888.5	1.633	1.445	
.573	0.327	906.9	1.726	1.564	
.500	0.311	925.3	1.808	1.645	
.432	0.281	954.5	1.925	1.742	
.407	0.276	971.1	1.980	1.785	
.368	0.254	990.8	2.030	1.868	
.308	0.198	1016.4	2.119	1.956	
.255	0.173	1041.0	2.166	2.077	
.239	0.153	1075.3	2.262	2.111	
.206	0.126	1100.7	2.326	2.223	
.164	0.080	1131.1	2.424	2.340	
.128	0.062	1166.5	2.523	2.470	
.100	0.004	1190.4	2.616	2.591	

5. Conclusions

One of the current results is associated with the relation between the planet's shape and its rotation profile. It has been seen that if the surface is more depressed than the spheroid i.e., when the surface is closer to the rotation axis of the mass distribution, the angular velocity increases from pole to the equator. This is due to the fact that the centripetal force at the surface increases rapidly from pole to the equator (section 4.2). And conversely, when the figure is more bloated than the spheroid, the centripetal force increases more slowly. According to equation (13), the radial force determines $\omega\,(r)$. Evidently, the gravitational force also depends on the mass distribution, so that we can expect that, under certain circumstances, the obtained results may not be valid. To see this, a three-shell model was constructed for Jupiter, in which the density decreased from the outermost layer to the central one. The surface distortion parameter *d* was positive (bloated surface). The resulting rotation profile had an increasing behavior from pole to the equator, contrary to the outcomes of section 4.1 and 4.2. Obviously, such a model is not realistic for a planet, and it is mentioned here as an extreme case that allows to see how a mass distribution can affect a rotation profile.

Rotation is perhaps a vastly common event in space. Planets rotate, some of them maybe differentially. Stars also rotate. There is evidence that stars (in the Kepler field) rotate with periods depending on the spectral type [15]. Moreover, Sun-like stars apparently rotate differentially [16, 17], and our Sun is not an exception, with the advantage that it can be observed in greater detail. Indeed, it is well-known that the Sun rotates with rates that change from pole to the equator [3, 18], specifically with $\omega_p = 1.98 \times 10^{-6}$ rad s^{-1} and $\omega_e = 2.88 \times 10^{-6}$ rad s^{-1}.

This resembles our models with a negative distortion parameter, but larger angular velocities. For instance, in the Saturn case with *d*=– 0.030, we have $\omega_p = 1.55 \times 10^{-4}$ rad s^{-1} and $\omega_e = 1.72 \times 10^{-4}$ rad s^{-1}.

However, another distinction between the two profiles is clear: the angular velocity of the Sun increases faster from pole to the equator than in Saturn, as shown in Figure 4.

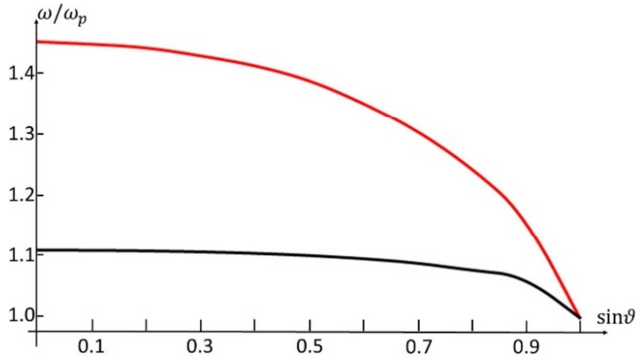

Figure 4. *Normalized angular velocity $\omega(\omega_p)^{-1}$ in dependence of the Sine of the latitude ϑ for: the Sun (red line) and for our Saturn model with d=-0.030 (black line).*

The two curves in Figure 4 are normalized to the corresponding polar angular velocity, so that at the pole: $\frac{\omega}{\omega_p} = 1\ (\sin\vartheta = 1)$.

We remark that, in our approach, it is tacitly admitted a pre-existing angular velocity, supported by a certain gravitational field, that sustains the equilibrium of the models. In other words, we are not searching for the dynamical process giving rise finally to a persistent rotation state and a determinate surface shape. For example, regarding the Sun, it is believed that differential rotation is the consequence of interaction between convection and solid-body rotation.

Appendix

Analytical expressions for determining the gravitational moments.

In terms of normalized variables, the integrals in (19) can be calculated by means of the functions:

$$f_0(e,z,x) = \frac{8\pi a^3 e^2 z}{15M(x+1)}(3x+2)$$

$$f_2(e,z,d) = \frac{8\pi a^3 e^2 z}{315M(x+1)^2}(2e^2(7x^2+10x+4) - 3(5x^2+7x+2)z^2)$$

$$f_4(e,z,d) = -\frac{8\pi a^3 e^2 z}{45045M(x+1)^3}(12e^4(77x^3+172x^2+140x+40) - 156e^2(15x^3+29x^2+18x+4)z^2 + 143\,(x+1)^2(7x+2)z^4)$$

$$f_6(e,z,d) = \frac{8\pi a^3 e^2 z}{153153M(x+1)^4}(8e^6(231x^4+708x^3+876x^2+504x+112) - 204e^4(39x^4+99x^3+96x^2+44x+8)z^2 \quad (39)$$

$$f_8(e,z,d) = -\frac{8\pi a^3 e^2 z}{2078505M(x+1)^5}(80e^8(209x^5+818x^4+1364x^3+1184x^2+528x+96) - 160e^6(663x^5+2115x^4+2808x^3+1972x^2+728x+112)z^2 + 2280e^4(x+1)^2(77x^3+92x^2+44x+8)z^4 - 2584e^2(x+1)^3\times(39x^2+22x+4)z^6 + 1615\,(x+1)^4(11x+2)z^8)$$

where $x=\sqrt{4d+1}$.

In the functions (A1), the factor $-1/Ma^{2n}$ appearing in

the definition of J_{2n} (equation (20)) is included.

References

[1] Cisneros, J. U., F. J. Martinez & D. Montalvo, 2019, ApJS, 241, 8.

[2] Cisneros, J. U., F. J. Martinez & D. Montalvo, 2020 American Journal of Astronomy and Astrophysics. Vol. 8, No. 1, 2020, pp. 8-14.

[3] Kitchatinov L. L., 2005, Physics-Uspekhi, 48 (5), 449.

[4] Sanchez-Lavega A., J. F. Rojas\ & P. V. Sada, (2000). Icarus 147, 405–420.

[5] Garcia-Melendo E., S. Pérez-Hoyos, A. Sánchez-Lavega \& R. Hueso, Icarus (2011) 215, 62–74.

[6] Helled, R., E. Galanti & Y. Kaspi, 2015, Nature 520, 202-204.

[7] Gudkova, T. V. & Zharkov, V. N., 1999, Planetary and Space Science, 47, 1211-1224.

[8] Cisneros, J. U., F. J. Martinez & D. Montalvo, 2017, ApJ, 848, 109.

[9] Cisneros, J. U., F. J. Martinez & D. Montalvo, RMxAA, 2016, 52, 375.

[10] Cisneros, J. U., F. J. Martinez, & D. Montalvo, American Journal of Astronomy and Astrophysics. Vol. 8, No. 2, 2020a, pp. 30-34.

[11] Bolton et al., 2017, Science 356, 821–825.

[12] Folkner, W. M. et al (2017), Geophys. Res. Lett, 44, 4694-4700.

[13] Durante, D., M. Parisi, D. Serra, et. al, (2020) Geophys. Res. Lett., 47 (4), e86572.

[14] Iess, L., B. Militzer, Y. Kaspi, et. al, (2019), Science, 364, 1052.

[15] Nielsen M. B., L. Gizon, H. Schunker & C. Karoff, 2013, A&A, 557, L10.

[16] Nielsen M. B., L. Gizon, H. Schunker & J. Schou, 2014, A&A, 568, L12.

[17] Nielsen M. B., L. Gizon, H. Schunker & W. H. Ball, 2015, A&A, 582, A10.

[18] Howard, R., J., M. Adkins et al 1983, Solar Phys. 83, 321.